JOURNAL OF ENGINEERING SCIENCES

Volume 12, Issue 2 (2025)

Kusyairi I., Choiron M. A., Purnowidodo A., Bintarto R. (2025). Optimizing Miura origami for enhanced energy absorption: A multi-objective approach. Journal of Engineering Sciences (Ukraine), Vol. 12(2), pp. D25–D44. https://doi.org/10.21272/jes.2025.12(2).d3

Optimizing Miura Origami for Enhanced Energy Absorption: A Multi-Objective Approach

Kusyairi I.[0009-0008-2055-6539], Choiron M. A.*[0000-0002-4052-4832], Purnowidodo A.[0000-0001-7312-4950], Bintarto R.[0000-0001-7209-9386]

Universitas Brawijaya, 8, Veteran St., 65145 Jawa Timur, Kota Malang, Indonesia

Article info:
Submitted: April 30, 2025
Received in revised form: July 23, 2025
Accepted for publication: August 7, 2025
Available online: August 27, 2025

***Corresponding email:**
agus_choiron@ub.ac.id

Abstract. This research addresses the critical challenge of improving structural energy absorption in crash scenarios. The study investigates the optimization of Miura origami-inspired thin-walled structures for vehicle safety systems. The structures were fabricated using AlSi10Mg aluminum alloy through selective laser melting (SLM) 3D printing technology. A frontal crash test scenario was simulated in ANSYS to assess structural performance under impact loading. The study applied a multi-objective optimization approach, combining the Taguchi method, principal component analysis (PCA), and composite desirability analysis, to evaluate the influence of design parameters such as wall thickness, number of sides, surface diameter, and number of segments. Based on the analysis of variance (ANOVA) results, wall thickness was identified as the most dominant factor, contributing 67 % to energy available (EA), while surface diameter and number of sides contributed 14 % and 7 %, respectively. The number of segments had a minor effect, contributing only 0.5 % to EA. The optimal configuration $t_3n_1d_3M_2$ was further validated through compression testing of 3D-printed prototypes, with deformation behavior analyzed using digital image correlation (DIC). The experimental findings closely matched simulation outcomes, confirming the robustness of the proposed optimization framework. These results provide valuable insights into integrating origami-inspired geometries and advanced additive manufacturing for enhanced crashworthiness in automotive structures.

Keywords: advanced manufacturing, sustainable design, high-strength aluminum alloy, selective laser melting, multi-objective optimization.

1 Introduction

Vehicle safety is a paramount concern in automotive engineering, relying heavily on the ability of structural components to absorb and dissipate impact energy during collisions. Thin-walled structures are commonly used in crash energy management systems due to their capability for controlled plastic deformation, which effectively absorbs kinetic energy. Traditional designs such as rectangular, circular, and multi-cellular thin-walled configurations have been widely studied, yet they often struggle to balance energy absorption efficiency, structural integrity, and weight constraints [1, 2].

Traditional designs such as rectangular, circular, and multi-cellular thin-walled configurations have been widely studied, yet they often struggle to balance energy absorption efficiency, structural integrity, and weight constraints [3].

To address these limitations, recent research has explored the integration of origami-inspired geometries into thin-walled structures. Among these, the Miura origami pattern stands out for its unique folding mechanism, which imparts compactness, high strength-to-weight ratios, and superior energy absorption capacity [4, 5]. The Miura pattern's ability to undergo extensive, controlled deformations without premature material failure makes it especially suitable for crashworthiness applications [6, 7]. Inflatable origami-based deployable structures have also been reviewed, demonstrating the broader applicability of origami in engineering [8].

At the same time, advancements in additive manufacturing, specifically selective laser melting (SLM), have enabled the production of complex geometries using advanced materials like AlSi10Mg, a lightweight aluminum alloy notable for its high strength and energy absorption capabilities [9]. Excellent fluidity and mechanical properties of AlSi10Mg make it ideal for intricate crashworthy structures fabricated via SLM [10].

Despite the promise shown by Miura origami thin-walled structures and SLM-fabricated AlSi10Mg

components, existing studies have been limited in their systematic optimization for automotive crash scenarios. Previous research often simplifies geometry, focuses on single performance criteria, or lacks comprehensive validation under realistic conditions [11]. Moreover, microstructural defects inherent to SLM-fabricated parts necessitate experimental validation to ensure simulation reliability [12].

Despite the promise shown by Miura origami thin-walled structures and SLM-fabricated AlSi10Mg components, existing studies have been limited in their systematic optimization for automotive crash scenarios. Previous research often simplifies geometry, focuses on single performance criteria, or lacks comprehensive validation under realistic conditions [11]. Moreover, microstructural defects inherent to SLM-fabricated parts necessitate experimental validation to ensure simulation reliability [12].

The intricate interdependence of geometric parameters (thickness, number of sides, surface diameter, and segment count) necessitates advanced multi-objective optimization methods to find optimal designs. Furthermore, manufacturing defects and microstructural inconsistencies in SLM-fabricated parts demand thorough experimental validation to ensure simulation accuracy and practical reliability [12]. The complexity of combining material behavior, geometry, and impact response under realistic crash conditions remains a significant challenge [11].

This study addresses these challenges by systematically optimizing the design of Miura origami thin-walled structures fabricated from AlSi10Mg using a multi-objective approach. Finite element analysis (FEA) simulations [13] evaluate crash performance, while experimental testing validates the results. The research integrates advanced statistical methods – including the Taguchi L27 orthogonal array [14, 15], principal component analysis (PCA) [16], and the composite desirability function (CDF) [17] – to optimize geometric parameters and maximize energy absorption, structural efficiency, and manufacturability. This comprehensive framework aims to advance the development of high-performance, crashworthy structural components for automotive safety applications by combining Miura origami designs, AlSi10Mg fabricated via SLM, and a robust multi-objective optimization and validation approach integrating simulation and experimental methods.

2 Literature Review

Thin-walled structures have become a primary focus in developing energy absorption systems for vehicle safety. The ability of these structures to absorb impact energy through controlled plastic deformation is crucial in mitigating collision impacts [18]. Recent studies have shown that structural geometries such as multi-cellular and origami patterns can significantly enhance energy absorption performance [19].

Developing effective energy absorption systems is central to advancing vehicle crashworthiness, with thin-walled structures remaining a widely adopted solution due to their ability to dissipate kinetic energy through controlled plastic deformation [20, 21]. Conventional geometries such as rectangular, circular, and multi-cellular profiles have been extensively studied for crash energy management. However, their performance is often constrained by limitations in deformation patterns, structural stiffness, and energy distribution under dynamic loads [22].

In response to these challenges, the field has increasingly explored origami-inspired engineering, where folded geometries enable structural elements to exhibit high flexibility, foldability, and superior energy absorption. Among the origami patterns investigated, the Miura fold has gained prominence due to its compact foldability, geometric adaptability, and ability to undergo large deformations without compromising material integrity [23]. Prior studies have shown that Miura origami enhances structural performance under axial and oblique loading by redistributing stress across multiple segments and delaying localized collapse [24, 25].

Parallel to geometric innovation, selecting suitable materials is pivotal in optimizing energy absorption. AlSi10Mg, a lightweight aluminum alloy, has emerged as a preferred material for impact-prone structures due to its high specific strength, ductility, and capacity for energy dissipation [26, 27]. The introduction of SLM has further enabled the precise fabrication of AlSi10Mg components with intricate geometries, offering unprecedented design flexibility for origami-based structures [28, 29]. Moreover, studies have confirmed that SLM-fabricated AlSi10Mg exhibits enhanced mechanical properties, including superior yield strength and fracture resistance, compared to conventionally processed counterparts [30].

However, while Miura origami structures and AlSi10Mg-based additive manufacturing have each demonstrated potential for energy absorption, limited research has combined both advances within a single design-to-evaluation framework. Additionally, few studies have applied systematic multi-objective optimization to the full design space of Miura structures, which involves complex parameter interactions (thickness, number of sides, surface diameter, and segment height). Traditional optimization approaches, often focusing on single-response functions, fail to capture the trade-offs necessary in real-world crash performance design [31].

To address this, recent efforts have turned to statistical design of experiments (DOE), such as the Taguchi method, to efficiently investigate multiple design variables while reducing the number of experiments [32]. Complementing this, PCA has been employed to reduce data dimensionality and reveal dominant response trends [33] while CDF integrates multiple conflicting objectives into a single optimization score [34]. These tools offer a promising pathway toward more balanced and performance-driven design solutions.

Finally, while FEA tools like ANSYS are widely used to simulate crash scenarios [35], experimental validation remains essential. Few studies have validated simulation results using digital image correlation (DIC) – a non-

contact optical method that provides high-resolution strain maps and reveals deformation behaviors in real-time [36]. Such triangulated validation (simulation, experimental testing, DIC) remains underutilized mainly in origami-based structures fabricated through additive manufacturing [37].

Despite advances in origami geometry, material science, and simulation techniques, no prior study has holistically integrated Miura origami design, AlSi10Mg via SLM, Taguchi/PCA/CDF-based multi-objective optimization, and comprehensive experimental validation (compression test and DIC). This represents a significant gap in the literature, particularly for automotive applications where maximizing energy absorption, crash resistance, and manufacturability must be addressed concurrently.

3 Research Methodology

3.1 Geometry

The geometry of the Miura origami thin-walled structure is a crucial element in understanding its mechanical behavior and potential for optimization in impact conditions. The Miura origami pattern is renowned for its unique folding mechanism, which imparts significant structural benefits such as a high strength-to-weight ratio and excellent energy absorption capabilities.

Figure 1 provides a comprehensive visualization of the Miura origami thin-walled structure.

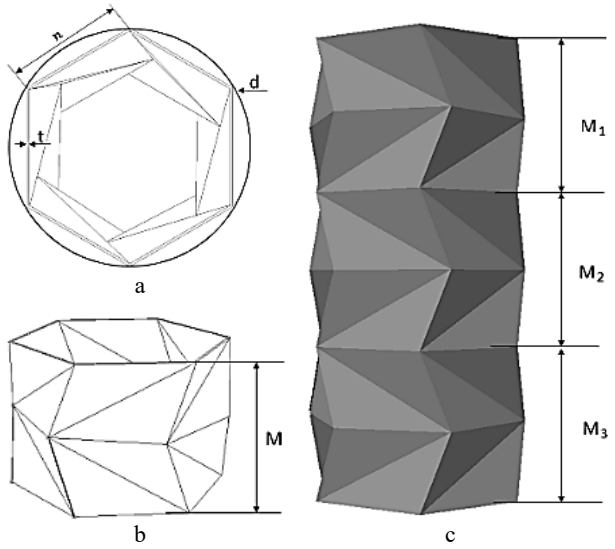

Figure 1 – Geometry of Miura origami thin-walled structures: a – the arrangement of the number of sides n, thickness t, and surface diameter d; b – a single segment of the thin-walled structure; c – a three-segment thin-walled structure

Figure 1 a presents a diagram illustrating the arrangement of the number of sides n, thickness t, and surface diameter d. The pattern consists of a series of interconnected parallelograms, where each internal angle θ is pivotal for the folding mechanism and overall structural integrity. The surface diameter d is defined as the distance between two opposite vertices on the perimeter of the origami unit and serves as a construction guide. The number of sides n will automatically adjust according to the diameter d of the guiding circle.

Figure 1 b shows a single segment of the thin-walled structure. This segment is the basic repeating unit of the Miura origami pattern, which can be stacked vertically to form more extensive structures. The height of the segment is determined by the folding pattern and the dimensions of the parallelograms, and it is a critical parameter in defining the overall height and mechanical properties of the structure.

Figure 1 c illustrates a three-segment thin-walled structure created by stacking three segments, as depicted in Figure 1 b. The structure's total height is the sum of the heights of the individual segments, denoted as M_1, M_2, and M_3, respectively. This modular configuration allows for flexibility in constructing structures of varying heights and complexities, making the Miura origami pattern highly versatile for engineering applications. The geometric parameters (i.e., the number of sides n, thickness t, surface diameter d, and segment height M) significantly determine the Miura origami thin-walled structures' mechanical properties and energy absorption capabilities. Manipulating these parameters optimizes the design to meet specific application requirements, such as enhancing crashworthiness in automotive components.

3.2 Material

The materials used in the Miura origami thin-walled structures are critical for ensuring optimal energy absorption and mechanical performance. This study selected AlSi10Mg, an aluminum alloy commonly employed in additive manufacturing via SLM, due to its superior mechanical properties and suitability for crash absorption applications. The material is fabricated using SLM and subjected to tensile testing per ASTM E8 standards. The results from the tensile tests are subsequently utilized for simulations to evaluate the material's performance in crash scenarios [38, 39].

Figure 2 illustrates the tensile test design used in this study, showing the specimen geometry and the setup for testing.

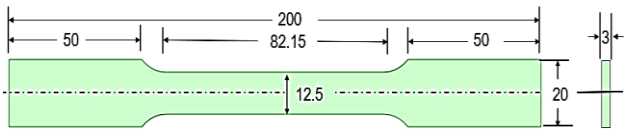

Figure 2 – Design Tensile ASTM E8 standard

Table 1 provides the key SLM printing parameters used to fabricate the AlSi10Mg specimens, essential for the structural simulations and analyses performed in this research [40, 41].

Figure 3 displays the stress-strain diagram obtained from the tensile test of AlSi10Mg, which highlights the material's behavior under axial loading.

Table 1 – SLM printing parameters

Parameter	Value
Support speed, mm/s	2600
Support power, W	200
Outer speed, mm/s	300
Outer power, W	270
Inskin speed, mm/s	1000
Inskin power, W	350
Downskin speed, mm/s	2000
Downskin power, W	240

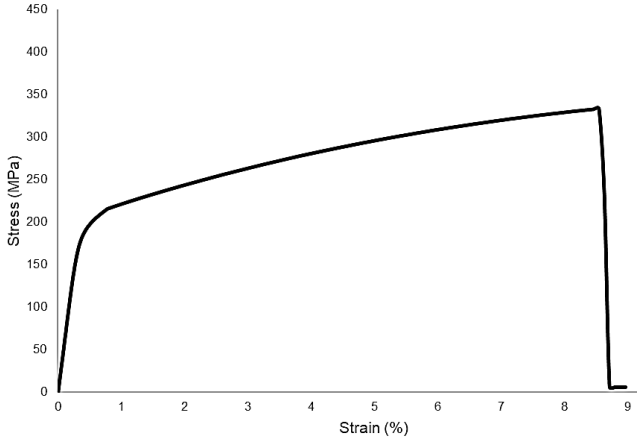

Figure 3 – Tensile strength for AlSi10Mg

This diagram is crucial for understanding the material's tensile properties, such as its ultimate tensile strength (UTS), yield strength, and elongation at break, which are integral to the simulation of crash scenarios using ANSYS software.

Table 2 shows material properties are fundamental for simulating crash scenarios using ANSYS software.

Table 2 – Material properties of AlSi10Mg

UTS, MPa	Young modulus, GPa	Yield strength, MPa	Elongation, %
352	48	219	8.5

AlSi10Mg, with its high tensile strength, adequate stiffness, and moderate elongation, is an ideal candidate for the Miura origami thin-walled structures designed to absorb energy efficiently during impact. The SLM process ensures precise material fabrication, allowing for intricate geometries that contribute to the structures' energy absorption capacity [42, 43].

The choice of AlSi10Mg is supported by its favorable mechanical performance, including its excellent strength-to-weight ratio and energy absorption characteristics, which are crucial for the structural integrity of the Miura origami designs. By leveraging the material properties of AlSi10Mg, this study aims to develop optimized Miura origami structures that can enhance vehicle safety in crash scenarios. These structures are designed to undergo significant deformation while effectively absorbing impact energy, thus improving crashworthiness. The potential of AlSi10Mg for energy absorption in crashworthy structures has been well-documented in the literature, highlighting its application in automotive safety and structural components that require high strength and energy absorption capabilities [44, 45]

3.3 Frontal crash test

The frontal crash test is a critical component of this study, designed to evaluate the energy absorption capacity and mechanical performance of Miura origami thin-walled structures. A frontal impact scenario was simulated using ANSYS Workbench 2023 R2, employing the Explicit Dynamics module with the LS-DYNA solver to capture transient dynamic responses and complex nonlinear deformation behaviors under low-speed crash conditions [46]. Pre-processing tasks, including meshing, boundary condition definition, and contact setup, were conducted using the ANSYS Mechanical module. The AlSi10Mg alloy was modeled with a bilinear isotropic hardening law calibrated from experimental stress-strain data to represent post-yield deformation accurately. The impactor was treated as a rigid body from structural steel to replicate realistic crash conditions.

As illustrated in Figure 4, the simulation replicates a low-speed frontal impact with an initial velocity of 2.22 m/s, consistent with FMVSS (Federal Motor Vehicle Safety Standards) crash protocols for bumper systems and energy-absorbing structures.

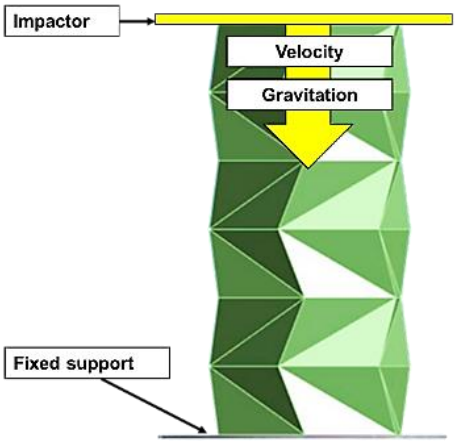

Figure 4 – Modelling simulation

The impactor moves vertically downward to compress the Miura origami structure axially, simulating an 80 mm crush zone to enable progressive folding and controlled deformation. The total simulation time was set to 36 ms, allowing the dynamic analysis to resolve time-dependent collapse behavior with high temporal accuracy [47].

Figure 5 illustrates the meshing strategy adopted for the Miura Origami structure and its interacting components.

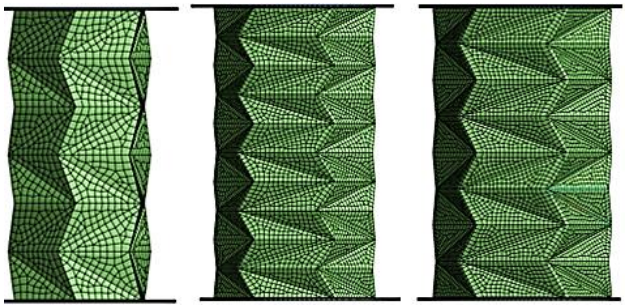

Figure 5 – Meshing Miura origami

The Miura Origami is modeled as a thin-walled structure composed of surface geometry, representing its folded configuration using shell elements. Accordingly, a face sizing mesh control was applied to ensure high-resolution meshing along the crease lines, fold transitions, and planar facets. This approach is critical for capturing local deformation modes, stress concentration zones, and the progressive folding behavior that governs energy absorption in origami-based systems. Face sizing allows for more precise element distribution along complex surface contours, essential in shell-type models where mechanical response is highly dependent on surface geometry fidelity [48].

In contrast, the impactor and fixed support plates were modeled as solid bodies exhibiting predominantly volumetric deformation. Therefore, body sizing generated three-dimensional elements that effectively capture stress propagation throughout the solid volume. Body sizing is particularly suitable for components undergoing rigid-body motion or internal stress wave transmission, where through-thickness accuracy and volumetric stiffness should be resolved adequately [49].

Table 3 reports the element quality metrics for nine Miura origami variants (A–I) to assess mesh integrity.

Table 3 – Mesh quality of Miura origami

Type	Element quality			
	Min	Max	Average	Standard deviation
A	0.41911	0.99998	0.96111	0.0502
B	0.54423	0.9998	0.94606	0.0608
C	0.45703	0.99977	0.94835	0.0606
D	0.42866	0.99985	0.95880	0.0567
E	0.42602	0.99991	0.95551	0.0512
F	0.42450	0.99987	0.95046	0.0541
G	0.41498	0.99999	0.95233	0.0540
H	0.49963	0.99974	0.95151	0.0656
I	0.43144	0.99995	0.95212	0.0523

All the configurations show a minimum element quality above 0.41, with the highest minimum in type B (0.5442), indicating the absence of degenerate or distorted elements. The average element quality consistently exceeds 0.94, with several types (A, D, E, G, and I) exceeding 0.95, confirming excellent mesh consistency for large-deformation and contact-based simulations. The low standard deviation values (less than 0.07) indicate uniform mesh quality distribution across each configuration.

As supported by best practices in computational mechanics, shell structures with an average element quality of more than 0.9 and a minimum of 0.4 are deemed reliable for nonlinear analysis, especially under impact or folding scenarios [49]. Hence, the meshing approach implemented (face sizing for surface-based origami and body sizing for volumetric components) is considered robust and appropriate for capturing the complex deformation mechanics of Miura Origami energy absorbers.

3.4 Performance metrics

Key performance metrics were evaluated to understand the crashworthiness of Miura origami thin-walled structures. The key performance metrics evaluated in this study include:

1) deformation patterns – the way the structure deforms under impact is crucial for understanding the energy absorption mechanisms;

2) energy available (EA) – the total energy absorbed by the structure during the impact. The energy absorption capacity of the Miura origami structure is determined using the following formula:

$$EA = \int_0^d F(x)dx \tag{1}$$

where EA – the total energy absorbed, J; x – displacement, m; $F(x)$ – the force applied, N; d = 0.08 m– the total deformation length;

3) specific energy absorption (SEA) – the energy absorbed per unit mass of the structure, J/kg:

$$SEA = \frac{EA}{m}, \tag{2}$$

where m – the mass of the structure, kg;

4) average force (AF) exerted on the structure during the impact, calculated by dividing the total energy absorption by the total deformation length, N:

$$F_{avg} = \frac{EA}{d}; \tag{3}$$

5) peak crushing force (PCF) – the maximum force experienced by the structure during the impact, which is a critical measure for evaluating the peak load-bearing capacity;

6) crush force efficiency (CFE) – the ratio of average force to peak crushing force, indicating the efficiency of the energy absorption process:

$$CFE = \frac{F_{avg}}{F_{max}}, \tag{4}$$

where F_{avg} – the average force, N; F_{max} – the peak crushing force, N.

The methodology and parameters for the frontal crash test are based on established practices in crashworthiness

studies and the mechanical properties of materials [50]. Various studies support the specific performance metrics and their importance.

3.5 Optimization methodology

The Taguchi method is employed in this study to optimize the design parameters of the Miura origami thin-walled structures for enhanced energy absorption and mechanical performance. The Taguchi method provides a systematic and efficient approach for determining the optimal settings of various parameters with a minimal number of experiments. This section describes the Taguchi L27 orthogonal array used for the optimization process.

Table 4 lists the specific design parameters, their symbols, units, and levels used in the optimization study for Miura origami thin-walled structures.

Table 4 – Levels of design parameters

Parameters	Parameter	Level		
		1	2	3
Thickness, mm	*t*	0.8	1.0	1.8
Number of sides	*n*	6	8	10
Diameter, mm	*d*	40	50	60
Segment	*M*	3	4	5

These parameters are varied to identify the optimal settings for enhanced energy absorption and mechanical performance using the Taguchi method.

Single-objective optimization is a critical process in engineering design, aiming to improve a specific performance metric of a structure while satisfying given constraints. In Miura origami thin-walled structures, single-objective optimization focuses on enhancing a particular response, such as EA, SEA, AF, PCF, or CFE. One effective method for performing single-objective optimization is the signal-to-noise (SN) ratio, which is a statistical measure used in the Taguchi method to determine the best levels of factors for robust performance. The SN ratio helps identify the optimal design parameters that minimize variability and enhance performance [14, 15].

The SN ratio is used to evaluate the performance characteristics of a design relative to variations in uncontrollable factors (noise). It converts the experimental results into a value for the optimization criterion, thus facilitating the identification of optimal conditions.

The SN ratio can be categorized into three types depending on the nature of the optimized response.

First, a larger-the-better SN ratio is used for responses where the goal is to maximize the value:

$$SN_{larger-the-better} = -10\,log\left(\frac{1}{n}\sum_{i=1}^{n}\frac{1}{y_1^2}\right). \quad (5)$$

where n – number of observations; y_1 – observed value of the response.

The larger-the-better SN ratio transforms the data into a logarithmic scale to emphasize the significance of larger response values while minimizing the effect of noise.

Second, a smaller-the-better SN ratio is used for responses where the goal is to minimize the value:

$$SN_{smaller-the-better} = -10\,log\left(\frac{1}{n}\sum_{i=1}^{n}y_1^2\right). \quad (6)$$

The smaller-the-better SN ratio is used when the goal is to minimize the response value, such as in minimizing peak forces [51].

Calculating the SN ratios for each response identifies the optimal design parameters for Miura origami thin-walled structures. The parameters that maximize the SN ratio for each response indicate the settings that lead to the best performance under varying conditions.

Analysis of variance (ANOVA) is a powerful statistical technique to identify the significant factors influencing an experiment's response variable. In optimizing Miura origami thin-walled structures, ANOVA is employed to analyze the experimental data obtained from the Taguchi method and determine the relative importance of different design parameters such as *t*, *n*, *d*, and *M*.

The desirability function $d_i(y)$ converts the response y into a scale from 0 (completely undesirable) to 1 (highly desirable). The function varies depending on whether the goal is to minimize, maximize, or reach a specific target:

$$d_i(smaller-the-better) = \begin{cases} 1,\ if\ y \le min\,y \\ \left(\frac{y-min\,y}{min\,y-max\,y}\right)^s,\ if\ min\,y \le y \le max\,y; \\ 0, if\ y \ge max\,y; \end{cases} \quad (7)$$

$$d_i(larger-the-better) = \begin{cases} 1,\ if\ y \le \min y; \\ \left(\frac{y-\max y}{\max y-\min y}\right)^s,\ if\ \min y \le y \le \max y; \\ 0, if\ y \ge \max y. \end{cases} \quad (8)$$

where $min\,y$ – the minimum acceptable value for the response (below this value, the desirability is 1, indicating a highly desirable outcome); $max\,y$ – the maximum acceptable value for the response (above this value, the desirability is 0, indicating an undesirable outcome); s – the shape factor that determines the curvature of the desirability function.

The part $\left(\frac{y-\max y}{\max y-\min y}\right)^s$ linearly decreases the desirability from 1 to 0 as the response value increases from $min\,y$ to $max\,y$.

These formulas help transform the response variable y into a desirability score ranging from 0 (completely undesirable) to 1 (highly desirable) based on minimizing or maximizing the response. The shape factor s controls how sharply desirability

changes between the minimum and maximum values.

The provided formula calculates the overall desirability D_i for a given treatment or experiment based on the individual desirabilities d_j of each response involved. This formula combines multiple responses into a composite measure that reflects overall performance. Here is a detailed explanation of the formula:

$$D_i = \prod_{j=1}^{n} d_j^{w_j}, \quad (9)$$

where D_i – the overall desirability for the i-th treatment; d_j – the desirability for the j-th response; w_j – the weight of each response such that $\sum_{j=1}^{n} w_j = 1$.

Formula (9) is a critical tool in multi-response optimization. By combining individual desirabilities from various responses, we can achieve a holistic view of the overall performance of a treatment or experiment. This facilitates decision-making to achieve optimal results [17, 52].

PCA is a sophisticated and comprehensive multivariate statistical approach widely used to derive relative weights in complex multi-optimization methodologies. This research uses PCA and CDF to identify optimal solutions. PCA converts a multi-objective problem into a single objective while preserving the distinct characteristics of the data. The detailed steps involved in PCA are as follows.

1) Step 1 (data normalization). The initial step involves normalizing the data based on maximization or minimization criteria. This ensures that all variables contribute equally to the analysis. The normalization process adjusts the data values to fall within a 0–1 range, as outlined by the normalization equations (7) and (8).

2) Step 2 (construction of the multi-response array). Following normalization, the composite desirability values d_i derived in step 1 are used to construct a multi-response array R. This array organizes the data such that each row corresponds to an observation, and each column corresponds to a different response variable. The array is structured as follows:

$$R = \begin{bmatrix} n_1(1) & n_1(2) & \dots & n_1(k) \\ n_2(1) & n_1(2) & \dots & n_2(k) \\ \vdots & \vdots & \ddots & \vdots \\ n_j(1) & n_j(2) & \dots & n_j(k) \end{bmatrix}. \quad (10)$$

3) Step 3 (developing the correlation coefficient matrix using the multi-response array R). The correlation coefficient matrix is constructed. This matrix captures the relationship between different response variables. The correlation between each pair of variables is calculated using the following formula:

$$M_{r,l} = \left(\frac{var(n_a(k), n_a(l))}{\sqrt{var(n_a(k))} \cdot \sqrt{var(n_a(l))}} \right), \quad (11)$$

where r, l – responses; k – number of variables.

The covariance and variance are used to standardize the relationships between the variables.

4) Step 4 (calculation of eigenvalues and eigenvectors). The next step involves calculating the eigenvalues λ_k and eigenvectors V_k of the correlation coefficient matrix. This is achieved by solving the characteristic equation:

$$(R - \lambda_k I) \cdot V_k = 0, \quad (12)$$

where I – the identity matrix.

Eigenvalues indicate the amount of variance captured by each principal component, while eigenvectors represent the directions of the principal components in the new feature space.

5) Step 5 (computation of principal components). Finally, the principal components Z_k are computed. Principal components are the uncorrelated variables that result from transforming the original dataset into the new feature space defined by the eigenvectors. The principal components are calculated using the following expression:

$$Z_k = \sum_{i=1}^{n} \eta_i(a) V_k. \quad (13)$$

This step ensures that the data is transformed into a set of uncorrelated components, with each component capturing as much variance as possible [16, 53, 54].

3.6 Research workflow overview

The research methodology (Figure 6) is structured into three phases: design, optimization, and experimental validation.

In the design phase, the process begins with structural modeling, followed by material testing to obtain the mechanical properties of the SLM-fabricated alloy. Using this data, key process parameters are determined and structured through the Taguchi L27 orthogonal array, which enables a systematic approach for evaluating multiple parameter combinations efficiently.

The Optimization Phase involves numerical simulations to predict the mechanical response under impact or compression. The results are analyzed through a multi-objective optimization strategy, from which the most suitable design configuration is selected as the optimized design. This design was fabricated via SLM 3D printing and evaluated in the experimental validation phase. Dimensional accuracy is assessed using 3D scanning, and mechanical performance is validated through quasi-static compression testing with DIC monitoring. Finally, numerical and experimental results are compared to validate the model's predictive accuracy and assess the effectiveness of the optimized design.

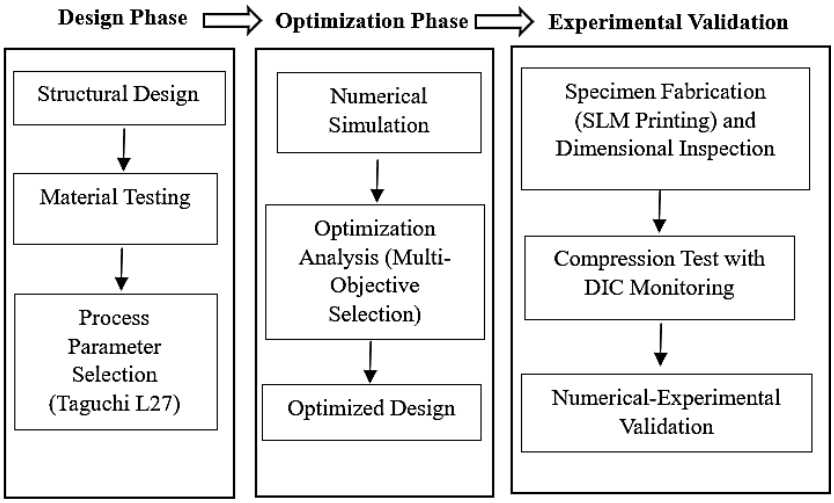

Figure 6 – Research workflow

4 Results

4.1 Deformation pattern

Their geometric configuration and material properties govern the deformation behavior of Miura origami thin-walled structures under compressive loading. Designed for crash energy absorption, these structures undergo controlled plastic deformation rather than elastic buckling, folding along predefined crease lines to dissipate energy progressively.

As seen in Table 5, variations in geometry significantly influence deformation modes and energy absorption performance.

Table 5 – Deformation patterns of Miura origami thin-walled structures under compressive loading

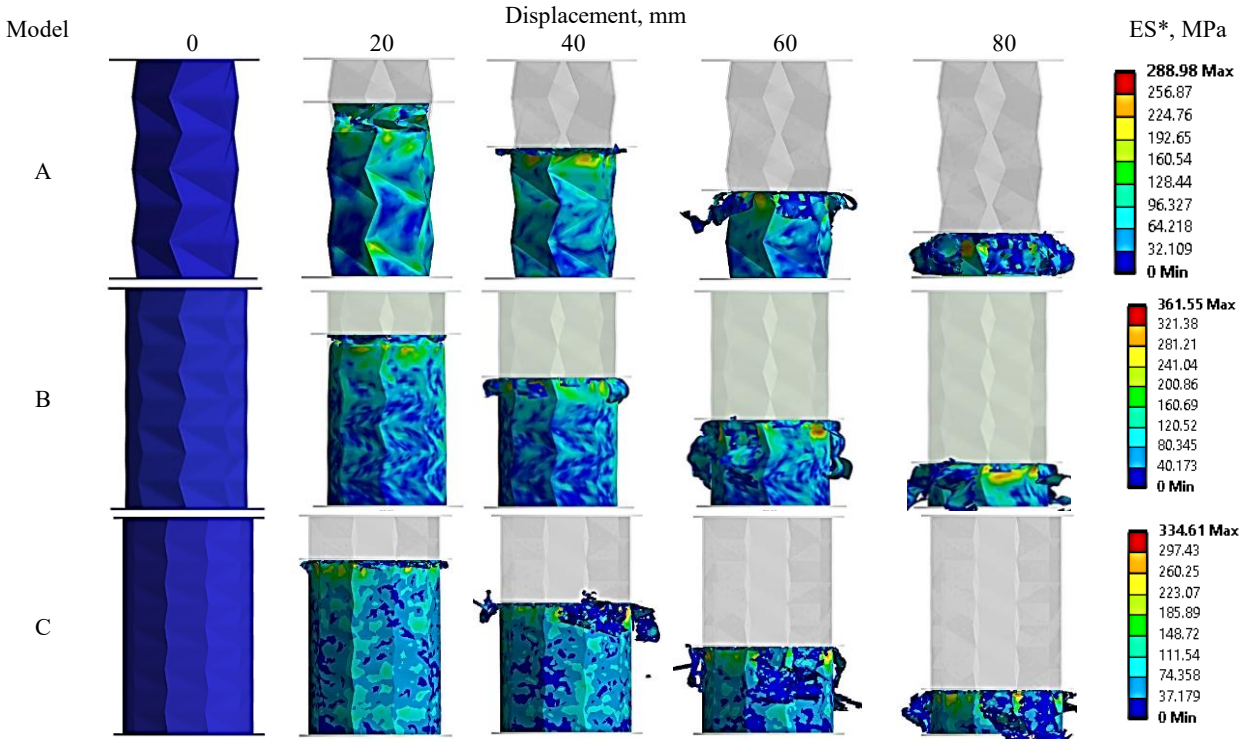

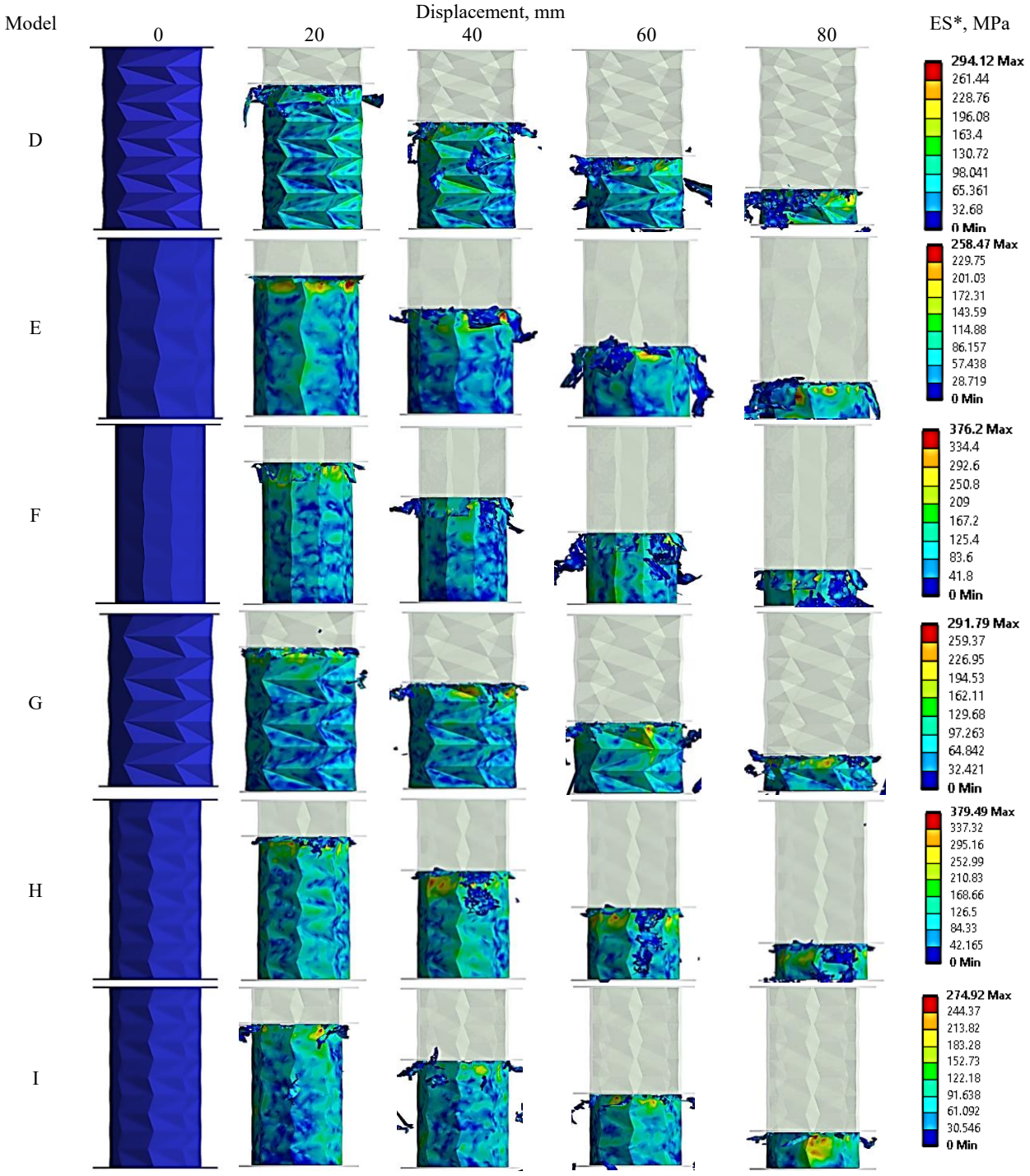

* ES – equivalent stress von Mises.

Model A, with the lowest thickness (0.8 mm), 6 sides, and 3 segments, exhibits rapid localized failure initiated at stress concentration zones such as hinge lines and panel junctions. This premature collapse results in poor energy absorption and low structural efficiency due to insufficient plastic hinge development.

In contrast, model C, maintaining the same thickness but featuring 10 sides, a larger diameter (60 mm), and 5 segments, shows gradual, distributed deformation. Enhanced geometric complexity facilitates progressive folding and multiple plastic hinge activations, leading to stable collapse and improved energy absorption with increased load-bearing capacity.

Models D, E, and F, with 1.0 mm thickness, display more uniform deformation patterns, resisting early folding. The increased wall thickness delays plastic flow onset and produces symmetric folding sequences, enhancing overall energy dissipation by effectively engaging the entire structure during compression.

Thicker models G, H, and I (1.8 mm) demonstrate increased rigidity and highly controlled deformation, resisting global collapse under higher compressive loads.

While this yields efficient energy absorption via stable hinge formation, the enhanced stiffness may reduce flexibility, potentially limiting rapid energy dissipation in specific impact scenarios. Across all configurations, deformation aligns with plastic folding theory, wherein plastic hinges form and propagate predictably along creases under axial loading. This ductile failure mode is essential for energy-absorbing components, especially those fabricated from ductile materials like AlSi10Mg, enabling substantial post-yield deformation and effective crash energy dissipation.

4.2 Energy metrics

EA is the total energy the structure absorbs during compression before failure.

In Table 6, model G (with 1.8 mm thickness, 6 sides, 60 mm side length, and 4 segments) shows the highest energy absorption value of 5.1 kJ, followed by model I (with 1.8 mm thickness, 10 sides, 50 mm side length, and 3 segments) at 3.6 kJ.

Table 6 – Design matrix and simulation result

No.	Model	Parameter				Response variables				
		t, mm	*n*	*d*, mm	*M*	*EA*, J	*SEA*, kJ/kg	*AF*, kN	*PCF*, kN	*CFE*, %
1	A	0.8	6	40	3	1110.8	33.7	13.9	9.84	1.4
2		0.8	6	40	3	930.11	28.2	11.6	8.77	1.3
3		0.8	6	40	3	1175.4	35.7	14.7	9.84	1.5
4	B	0.8	8	50	4	1385.4	38.2	17.3	9.87	1.8
5		0.8	8	50	4	1259.9	34.8	15.7	9.44	1.7
6		0.8	8	50	4	703.23	19.4	8.8	18.63	0.5
7	C	0.8	10	60	5	1316.9	33.2	16.5	29.81	0.6
8		0.8	10	60	5	1324.5	33.4	16.6	29.74	0.6
9		0.8	10	60	5	1008.5	25.4	12.6	29.74	0.4
10	D	1.0	6	50	5	1412.4	29.4	17.7	8.86	2.0
11		1.0	6	50	5	1412.4	29.4	17.7	8.86	2.0
12		1.0	6	50	5	1394.7	29.0	17.4	8.86	2.0
13	E	1.0	8	60	3	1962.9	39.8	24.5	29.19	0.8
14		1.0	8	60	3	2086.3	42.3	26.1	29.19	0.9
15		1.0	8	60	3	2140.1	43.4	26.8	29.16	0.9
16	F	1.0	10	40	4	1120.5	27.1	14.0	34.25	0.4
17		1.0	10	40	4	1040.0	25.2	13.0	33.36	0.4
18		1.0	10	40	4	1089.4	26.4	13.6	33.36	0.4
19	G	1.8	6	60	4	5085.9	54.9	63.6	31.56	2.0
20		1.8	6	60	4	4826.5	52.1	60.3	37.01	1.6
21		1.8	6	60	4	4454.6	48.1	55.7	31.55	1.8
22	H	1.8	8	40	5	2623.8	35.3	32.8	65.21	0.5
23		1.8	8	40	5	2623.8	35.3	32.8	42.74	0.8
24		1.8	8	40	5	2623.8	35.3	32.8	42.74	0.8
25	I	1.8	10	50	3	2214.8	27.1	27.7	80.30	0.3
26		1.8	10	50	3	3645.1	44.6	45.6	83.99	0.5
27		1.8	10	50	3	2271.6	27.8	28.4	83.24	0.3

These models exhibit significant energy absorption due to the combination of higher material thickness and more complex folding patterns.

Model G, with its thicker material (1.8 mm), has the highest energy absorption of all the models. This is primarily due to the increased stiffness of the material, which helps the structure resist early failure and continue absorbing energy throughout the deformation process.

Model I, while having the same thickness as model G, also demonstrates a high level of energy absorption. However, it has a slightly lower CFE (0.34%) than model G, indicating that it does not distribute the absorbed energy as efficiently across the structure.

Models with thinner materials, such as models A and B (0.8 mm thickness), have lower energy absorption values (1.2 kJ and 0.7 kJ, respectively). The reduced energy absorption is due to the material's lower stiffness and decreased ability to resist deformation under high compression.

SEA is an important metric that measures how much energy the structure can absorb per unit mass. This is useful for evaluating energy absorption efficiency relative to material weight. The SEA values vary significantly across different models:

– model G, with 1.8 mm thickness, 8 sides, and 60 mm diameter, records the highest SEA value at 54.9 kJ/kg, indicating that this configuration provides exceptional energy absorption efficiency. This is due to a favorable combination of geometry

and wall thickness that optimally balances structural stiffness and deformability;

– model H, with identical parameters to model G, also shows a very high SEA value of 52.1 kJ/kg, suggesting consistency and reliability in performance for this configuration;

– model F, previously identified as high-performing, achieves a SEA of 26.3 kJ/kg, much lower than models G and H. This indicates that although F performs well, it is not the most efficient when energy absorption is normalized to mass;

– model A, with thinner walls (0.8 mm), has a decent SEA of 35.7 kJ/kg, which reflects its limited absolute energy absorption capacity due to lower structural mass and simpler geometry.

CFE is a critical indicator of how efficiently the structure dissipates compressive energy. Higher CFE means better conversion of compressive forces into absorbed energy, minimizing destructive transfer:

– model G again leads with a CFE of 2.0 %, the highest among all models, showing not only high energy absorption but also excellent force dissipation capacity;

– model H follows closely with a CFE of 1.6 %, reinforcing the superior performance of thick-walled and geometrically complex configurations;

– model I, despite its relatively high SEA (up to 35.3 kJ/kg in some configurations), exhibits the lowest CFE at 0.3 %, indicating inefficient force conversion and suggesting susceptibility to localized failure or excessive stiffness that limits ductile deformation;

– model D, with moderate thickness (1.0 mm) and 6 sides, has a CFE of 2.0 %, indicating a good balance of structural stiffness and energy dissipation capability.

4.3 ANOVA results

The ANOVA was conducted to assess the relative influence of each design parameter on the response variables, including EA, SEA, PCF, and CFE (Table 7).

The results from the ANOVA provide valuable insights into how *t*, *n*, *d*, and *M* affect the overall performance of Miura origami thin-walled structures under compressive loads.

The *t* emerged as the most influential factor across all response variables, with significant contributions of 67 % to EA, 21 % to SEA, and 67 % to both AF and PCF. The high F-values and low P-values for thickness indicate that they play a pivotal role in determining the energy absorption capacity and the structural stability of the material.

Thicker materials provide greater resistance to deformation and buckling, thereby improving both energy absorption and structural strength during compression.

The parameter *n* is the number of polygonal sides in the cross-sectional profile. It was found to influence EA at 14 % moderately and had a minor impact on AF and PCF at 7 % each. However, it showed a dominant contribution to CFE, reaching 75 %. This indicates that increasing the number of sides in the cross-section enhances geometric complexity, promoting more uniform force distribution and efficient deformation under axial loading. Although the effect on absolute energy metrics (such as EA and AF) is modest, the improved load-sharing capacity contributes substantially to the structure's energy dissipation efficiency.

Table 7 – ANOVA result values

Resp.	Source	Adj SS	F-value	P-value	Contr.
EA	*t*, mm	$2.58 \cdot 10^7$	131.3	0	67.4
	n	$2.55 \cdot 10^6$	13.0	0.002	6.7
	d, mm	$5.41 \cdot 10^6$	27.5	0.000	14.1
	M	$1.79 \cdot 10^5$	0.9	0.350	0.5
	Error	$4.32 \cdot 10^6$	n/a*	n/a	n/a
	Total	$3.83 \cdot 10^7$	n/a	n/a	n/a
SEA	*t*, mm	$4.04 \cdot 10^2$	12.1	0.002	20.8
	n	$2.75 \cdot 10^2$	8.2	0.009	14.1
	d, mm	$4.54 \cdot 10^2$	13.6	0.001	23.4
	M	$0.76 \cdot 10^2$	2.3	0.146	3.9
	Error	$7.33 \cdot 10^2$	n/a	n/a	n/a
	Total	$1.94 \cdot 10^3$	n/a	n/a	n/a
AF	*t*, mm	$4.03 \cdot 10^9$	131.3	0.000	67.4
	n	$3.98 \cdot 10^8$	13.0	0.002	6.7
	d, mm	$8.45 \cdot 10^8$	27.5	0.000	14.1
	M	$2.80 \cdot 10^7$	0.9	0.350	0.5
	Error	$6.76 \cdot 10^8$	n/a	n/a	n/a
	Total	$5.98 \cdot 10^9$	n/a	n/a	n/a
PCF	*t*, mm	$7.44 \cdot 10^9$	169.5	0.000	67.4
	n	$4.44 \cdot 10^9$	101.0	0.000	6.7
	d, mm	$5.50 \cdot 10^5$	0.01	0.912	14.1
	M	$5.22 \cdot 10^8$	11.9	0.002	0.5
	Error	$9.66 \cdot 10^8$	n/a	n/a	n/a
	Total	$1.34 \cdot 10^{10}$	n/a	n/a	n/a
CFE	*t*, mm	$7.63 \cdot 10^{-2}$	0.8	0.371	0.8
	n	7.51	82.1	0.000	75.4
	d, mm	0.25	2.7	0.113	2.5
	M	0.11	1.2	0.282	1.1
	Error	2.01	n/a	n/a	n/a
	Total	9.96	n/a	n/a	n/a

* Not applicable.

The parameter *d* demonstrated a moderate influence across the evaluated responses. It contributed 14 % to EA, 23 % to SEA, and 14 % each to AF and PCF. These values indicate that while *d* affects deformation capacity and load-bearing characteristics, its role remains secondary compared to more dominant factors such as *t* and *n*. Nevertheless, adjustments in d can enhance foldability and geometric response and support improved energy dissipation when combined with optimized structural configurations.

The parameter *M* was found to have a relatively small influence on all response variables. It contributed only 0.5 % to EA, AF, PCF, and 1.1 % to CFE. However, its impact on SEA was more noticeable, contributing 3.9 %. This suggests that while increasing the number of segments can promote more distributed folding and improve energy absorption efficiency relative to mass, it

has a limited effect on the structure's absolute load-bearing capacity. Therefore, the segment number should be considered a secondary design factor and best optimized with more dominant parameters such as wall thickness and polygonal side count.

In conclusion, the ANOVA results confirm that *t* is the most influential parameter, significantly affecting energy absorption, force distribution, and structural stability in Miura origami thin-walled structures.

Parameters *n* and *d* also play important roles, particularly in folding behavior and deformation control. In contrast, parameter *M* has a relatively minor effect, contributing primarily to SEA rather than overall structural strength. These insights serve as a valuable basis for optimizing origami-inspired energy absorbers, emphasizing the importance of thickness and geometric complexity in achieving superior crash performance.

4.4 Single-response optimization

Table 8 shows the results of single-response optimization for Miura origami thin-walled structures, detailing the optimal settings for individual responses: EA, SEA, AF, PCF, and CFE.

Table 8 – SN ratio values of response variables

Model	EA	SEA	AF	PCF	CFE
A	60.47	30.12	82.41	–79.55	2.95
B	59.76	28.57	81.69	–82.50	–2.37
C	61.49	29.52	83.43	–89.47	–6.05
D	62.96	29.32	84.90	–78.95	5.95*
E	66.27	32.41	88.21	–89.30	–1.09
F	60.68	28.37	82.62	–90.54	–7.92
G	73.57*	34.24*	95.50*	–90.49	5.02
H	68.38	30.95	90.32	–94.21	–3.89
I	68.02	29.78	89.96	–98.33*	–8.33
Optimal level	$t_3n_1d_3M_2$	$t_3n_1d_3M_2$	$t_3n_1d_3M_2$	$t_3n_3d_2M_1$	$t_2n_1d_2M_3$

* Optimized setting of individual responses.

These results reveal the most effective parameter configurations for maximizing or minimizing each response, thus providing insights into the structural performance of the Miura origami designs. Single responses were optimized based on SN ratios using the "larger-is-better" criterion for EA, SEA, AF, and CFE, and the "smaller-is-better" criterion for PCF.

Applying the SN ratio approach identified the optimal levels for each response, highlighting the best parameter combinations to achieve superior energy absorption, force distribution, and crashworthiness performance. This optimization process is crucial for designing Miura origami structures capable of efficiently absorbing impact energy while maintaining high stability and force resistance during compression. The study provides the following optimized settings for each response: EA, SEA, AF for $t_3n_1d_3M_2$, PCF for $t_3n_3d_2M_1$, and CFE for $t_2n_1d_2M_3$. These optimal parameter settings, derived from the single-response optimization process, demonstrate how the combination of *t*, *n*, *d*, and *M* can be fine-tuned to achieve the desired performance characteristics in Miura origami thin-walled structures.

4.5 Multi-objective optimization

Table 9 presents the PCA results conducted to reduce the dimensionality of the multi-response dataset in the optimization of Miura origami thin-walled structures. PCA transforms a set of correlated variables into a smaller number of uncorrelated principal components (PC), each representing a direction of maximum variance in the data.

Table 9 – Principal component analysis

Component	PC1	PC2	PC3	PC4	PC5
Eigenvalue	3.366	1.428	0.131	0.075	0.000
Proportion	0.673	0.286	0.026	0.015	0.000
Cumulative	0.673	0.959	0.985	1.000	1.000
Eigenvectors	0.540	0.026	–0.056	0.452	0.707
	0.522	0.059	0.652	–0.547	0.000
	0.540	0.026	–0.056	0.452	–0.707
	–0.323	0.646	0.552	0.418	0.000
	0.197	0.760	–0.515	–0.344	0.000

In this study, five components were extracted, with PC1 and PC2 capturing the most significant portion of the variability (67 % and 29 %, respectively), leading to a cumulative variance of 96 %. This indicates that these two components are sufficient to represent the key information within the original multi-response dataset.

The eigenvectors show how strongly each performance variable contributes to the principal components. PC1 represents the dominant performance trend, while PC2 captures an orthogonal secondary trend. Since PC3 to PC5 contribute only 2.6 %, 1.5 %, and 0.0 %, respectively, they are considered less influential and likely contain redundant or noise-related information. Focusing on PC1 and PC2 simplifies the optimization process while retaining most meaningful data variance, making it suitable for robust multi-objective decision-making.

The PCA results confirm that PC1 and PC2 sufficiently represent the critical variations among the evaluated responses. This dimensionality reduction facilitates a more efficient and integrated multi-objective optimization process by focusing on these key components instead of numerous individual metrics.

Table 10 presents the composite desirability values for each model regarding the response variables. These composite values are derived by combining the individual desirability for each response variable, providing an overall measure of performance for each model. Higher composite desirability values indicate better overall performance based on the desired objectives. The composite desirability data for each model reflects the trade-offs between maximizing positive responses (such as EA, SEA, AF) and minimizing undesirable ones (such as PCF and CFE). The values range from 0 (poor performance) to 1 (optimal performance), indicating how well each model meets the performance targets across all responses.

Table 10 – Composite desirability values

Model	Composite desirability data				
	EA	SEA	AF	PCF	CFE
A	0.0518	0.2487	0.0518	1.0000	0.5708
B	0.0000	0.0000	0.0000	0.8689	0.0391
C	0.1400	0.3886	0.1400	0.7203	0.0892
D	0.1618	0.2809	0.1618	0.9989	0.9870
E	0.3279	0.6753	0.3279	0.7289	0.3167
F	0.0952	0.2180	0.0952	0.6613	0.0000
G	1.0000	1.0000	1.0000	0.6970	1.0000
H	0.4382	0.4475	0.4382	0.5485	0.2233
I	0.6713	0.7092	0.6713	0.0000	0.0832

Table 11 presents the Weighted Composite Desirability Values for each Miura origami model across five key performance responses: EA, SEA, AF, PCF, and CFE.

Table 11 – Weighted composite desirability values

No.	Weighted CDF					P-CDF	Rank
	EA	SEA	AF	PCF	CFE		
A	0.422	0.684	0.422	1.000	0.978	0.119	6
B	0.000	0.000	0.000	0.985	0.882	0.000	7
C	0.564	0.773	0.564	0.966	0.910	0.216	5
D	0.588	0.708	0.588	1.000	0.999	0.244	4
E	0.722	0.899	0.722	0.968	0.956	0.434	3
F	0.504	0.660	0.504	0.958	0.000	0.000	7
G	1.000	1.000	1.000	0.963	1.000	0.963	1
H	0.786	0.803	0.786	0.939	0.943	0.440	2
I	0.890	0.911	0.890	0.000	0.908	0.000	7

These values account for the relative importance of each response variable based on design objectives and are used to compute a P-CDF score, which reflects the aggregated desirability of each model. The P-CDF value determines the final ranking, where a higher score denotes better overall crashworthiness and energy absorption performance.

The analysis shows that model G ranks highest (P-CDF = 0.963), achieving perfect desirability scores (1.000) in all five metrics, making it the most optimal configuration for energy-absorbing applications. Model H ranks second (P-CDF = 0.440), with strong but slightly lower values in PCF and CFE. Model E follows in third place (P-CDF = 0.434), indicating a balanced performance across all parameters. In contrast, models B, F, and I rank lowest due to poor performance in critical criteria (e.g., EA, SEA, AF in models B and I) or inconsistencies across responses. Despite showing strong values in CFE and PCF, Model D is ranked fourth due to lower composite desirability in SEA. This highlights how P-CDF offers a more holistic assessment than evaluating individual metrics alone.

The optimal levels identified in the multi-objective optimization, as presented in Table 12, align with those from the single-response optimization. The combination $t_3n_1d_3M_2$ consistently emerges as the optimal design configuration, confirming its effectiveness in enhancing the performance of Miura origami thin-walled structures across multiple responses.

Table 12 – Optimal conditions for attaining multi-optimization

Level	Response table for means			
	t, mm	*n*	*d*, mm	*M*
1	0.112	0.442*	0.186	0.184
2	0.226	0.291	0.081	0.321*
3	0.468*	0.072	0.538*	0.300
Delta	0.356	0.370	0.456	0.137
Rank	3	2	1	4

*Optimal levels of multi-objective optimization

The multi-objective optimization results support the single-response optimization and weighted composite desirability analysis findings. The optimal configuration $t_3n_1d_3M_2$ provides the best overall performance, effectively balancing the trade-offs between different response variables such as EA, SEA, AF, PCF, and CFE. The integrated analysis confirms that the third level of thickness, first level of number of sides, third level of surface diameter, and second level of number of segments ($t_3n_1d_3M_2$) form the most optimal combination for designing Miura origami thin-walled structures. This configuration maximizes energy absorption and mechanical efficiency, making it highly suitable for applications requiring enhanced crashworthiness and structural performance. The consistency across various optimization methods underscores the robustness of these findings, providing a reliable foundation for future design and development of advanced origami-based structures.

4.6 Experimental results

Figure 7 illustrates the dimensional inspection process of specimens fabricated via SLM using the FARO Quantum Max 3D laser scanner.

Figure 7 – 3D scanning setup using FARO Quantum Max

A blue laser line is projected onto the specimen surface while the articulated arm is manually maneuvered to capture its geometry comprehensively. This non-contact scanning technique is particularly suited for verifying thin-walled and geometrically complex structures such as origami-inspired designs. Before scanning, each specimen was coated with a thin layer of anti-reflective developer spray to minimize laser scattering. Multiple scanning

passes were performed from various angles to ensure complete surface coverage, including folded and recessed regions. The acquired point cloud data were converted into STL format and used as the basis for dimensional deviation analysis against the original CAD model.

Dimensional evaluation was carried out using Geomagic Control X software, in which the scanned mesh was aligned with the nominal CAD model using a best-fit alignment algorithm. This process enabled the generation of color-coded deviation maps to represent surface discrepancies visually. With a form accuracy of 26 µm, point spacing of 13 µm, and a measurement uncertainty of approximately 31 µm, the scanner provides high-resolution capability for assessing surface quality, feature sharpness, and structural conformity.

In Figure 8, the comparison between the CAD model and the SLM-printed Miura origami reveals notable differences in dimensional fidelity across various regions.

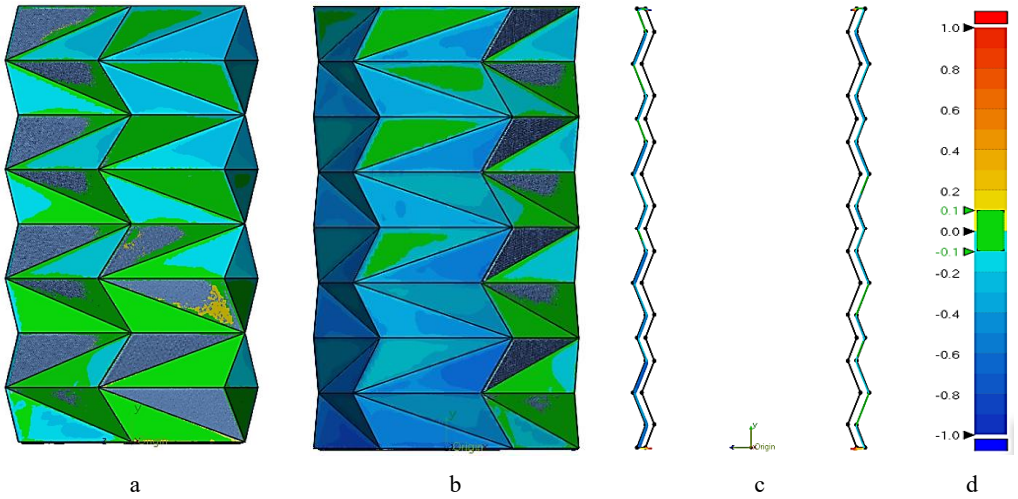

Figure 8 – Comparison of CAD model and SLM-printed Miura origami: a – front view; b – back view; c – thickness; d – deviation

The rear section, characterized by thicker material, exhibits superior dimensional stability throughout the printing process. These denser regions are less susceptible to thermal shrinkage, resulting in improved geometric consistency. This effect may be attributed to more uniform laser exposure during the SLM process, which reduces localized thermal gradients. In contrast, the Miura structure, which incorporates complex fold geometries, shows more pronounced dimensional deviations at sharp fold corners. These deviations are primarily attributed to localized thermal stresses generated during layer solidification.

Although deviations up to ±1.0 mm are theoretically possible, the measured dimensional discrepancies remain within a more realistic and acceptable range, typically between ±0.2 mm and ±0.5 mm. These values fall well within the tolerances required for most engineering applications, indicating satisfactory dimensional fidelity of the SLM-fabricated structure. Most of the geometry exhibits deviations between ±0.1 mm and ±0.3 mm, with fold corners occasionally reaching ±0.4 mm to ±0.5 mm, particularly in regions with thin walls or abrupt curvature transitions.

The deviation map further indicates that central regions and structurally reinforced zones exhibit minimal deviations (less than ±0.2 mm), suggesting effective heat dissipation and mechanical anchoring during fabrication. Conversely, moderately complex regions show deviations up to ±0.4 mm, consistent with increased geometric sensitivity under SLM conditions. Overall, the dimensional accuracy remains within acceptable industrial tolerances; however, specific zones (particularly at thin fold intersections) highlight the need for continued optimization of scanning strategies, laser exposure parameters, and thermal management during the additive manufacturing of complex origami-based thin-walled structures.

The experimental setup for this study employs a DIC system to measure full-field strain and displacement during quasi-static compression testing of thin-walled specimens. DIC is a non-contact optical technique that captures surface deformation by tracking a random speckle pattern on the specimen through high-resolution sequential imaging. This technique provides precise, full-field visualization of deformation, essential for validating numerical models and understanding the mechanical behavior of complex geometries.

As shown in Figure 9, the DIC system consists of several key components.

Figure 9 – Setup of compression test with DIC monitoring

Point A identifies the high-speed camera, specifically a Phantom VEO model, equipped with a Canon EF 50 mm f/1.4 lens. This configuration allows for high temporal and spatial resolution, which is suitable for capturing rapid deformation events with excellent clarity. The camera faces the specimen perpendicularly, recording surface deformations with minimal distortion. Adequate illumination is also provided to maximize speckle pattern contrast for accurate correlation. Point B refers to the universal testing machine (UTM), which applies a controlled compressive load to the specimen under quasi-static conditions. The UTM has a high-precision load cell and a displacement sensor to record force and axial movement during the test. The machine is synchronized with the camera using a trigger system to ensure that mechanical data and image acquisition are temporally aligned.

Point C shows the computer connected to the UTM, which is used to operate the testing machine, record real-time force–displacement data, and monitor test progress. This data is critical for correlating the mechanical response of the specimen with the optical strain measurements obtained from DIC. Point D marks the computer workstation dedicated to DIC image processing, which operates the Phantom camera using Phantom Camera Control (PCC) software and performs post-processing with MicroVec DIC software. The PCC software enables real-time configuration of frame rate, exposure time, resolution, and trigger parameters. After data acquisition, the image sequences are exported and analyzed using MicroVec to compute full-field displacement and strain distributions. The software detects sub-pixel movement in the speckle pattern and generates maps highlighting strain localization, folding mechanisms, and potential failure initiation. This comprehensive and synchronized setup allows for accurate tracking of structural deformation and serves as a robust tool for experimental validation of numerical simulations and for studying complex behaviors in thin-walled structures.

The compression test of a thin-walled structure fabricated from AlSi10Mg alloy using SLM at a testing speed of 20 mm/s provides valuable insights into the material's deformation and failure mechanisms under compressive loading. The material's performance is closely tied to the microstructural features induced during the SLM process, such as porosity, residual stresses, and anisotropic behavior, which may significantly influence the mechanical response of the component during testing.

Figure 10 compares the force–deformation responses obtained from experimental testing and numerical simulation. The blue curve represents the experimental results under quasi-static compression, while the orange curve depicts the simulation results conducted using a dynamic drop test setup.

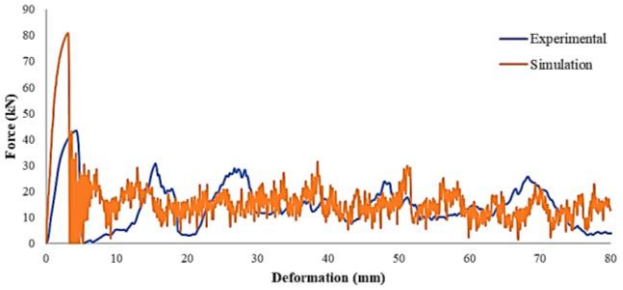

Figure 10 – Force reaction

Both datasets reflect the thin-walled structure's progressive deformation and energy absorption characteristics. Despite differences in peak force magnitude and fluctuation intensity (primarily due to variations in loading rate and boundary conditions) the two curves exhibit a generally consistent deformation pattern. Both show similar stages of initial stiffness, localized folding, and post-buckling collapse. This similarity in force trends indicates that the numerical model successfully captures the mechanical behavior of the specimen under compression. Quantitatively, the EA derived from the area under the force–deformation curves shows a close match, with only a 3 % difference between the experimental and simulation results. This slight discrepancy further confirms that, while the simulation uses a different loading condition, it remains reliable for approximating structural performance and energy dissipation capacity.

At the onset of the test, the force increases sharply with the displacement, reaching an initial peak around 5 mm. This behavior indicates the material's resistance to elastic deformation, where the thin-walled AlSi10Mg structure behaves predominantly elastically, displaying an initial stiffness. This phase is marked by the material's ability to withstand compressive forces without significant plastic deformation. However, the rapid initial rise in force suggests that the material exhibits limited ductility, a characteristic often observed in metallic alloys, especially those with high silicon content such as AlSi10Mg.

In Figure 10, the force-deformation curve shows an initial sharp peak at approximately 6 mm, followed by a rapid force drop, indicating the onset of localized plastic deformation or yielding. This behavior is characteristic of thin-walled structures produced via SLM, where residual porosity, microstructural anisotropy, and lack-of-fusion defects act as stress concentrators, reducing the effective load-bearing capacity.

Subsequent fluctuations at around 15 and 25 mm suggest sequential localized failure events, such as buckling or fracture initiation at critical fold lines or defect sites. These multiple peaks highlight the progressive collapse typical of additively manufactured structures, where stress redistribution leads to repeated local failure rather than a single catastrophic collapse.

After 68 mm of deformation, the force continues to decline steadily, marking the final collapse stage of the

specimen. This behavior suggests a brittle-to-ductile transition, influenced by the absence of heat treatment and the inherent brittleness of as-built AlSi10Mg. The experimental curve consistently shows lower peak forces and greater noise than the simulation, indicating real-world imperfections not captured in the idealized model. This emphasizes the need for defect mitigation through process optimization or post-processing to improve the mechanical performance of thin-walled structures.

Figure 11 illustrates a three-way comparison of deformation behavior in Miura origami thin-walled structures under compressive loading: finite element simulation (left column), experimental observation (middle), and DIC mapping (right).

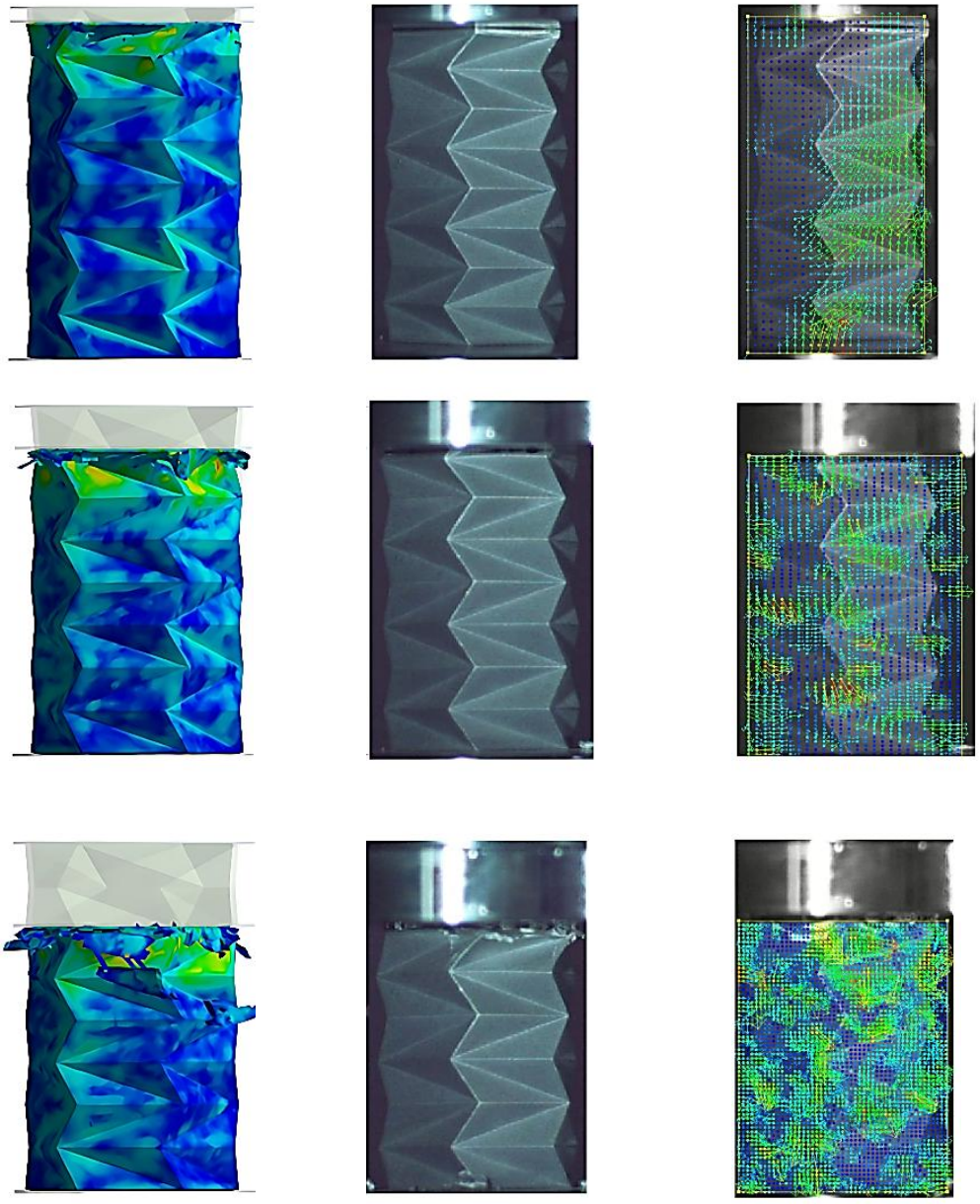

a b c

Figure 11 – Comparison of deformation analysis results: a – numerical simulations; b – physical experimentation; c – DIC.

These sequential stages capture the progression from initial contact to near-total collapse, offering critical insights into the numerical model's structural mechanics and accuracy.

In the first row, representing the early deformation stage, all three modalities show uniform surface geometry with minimal folding. In the DIC image, arrow vectors align along the prefolded creases of the Miura pattern, particularly in the midsection, indicating the structure's tendency to deform along the predefined fold lines. This behavior is consistent with the simulation results, where stress is distributed symmetrically and remains concentrated at hinge intersections. The minimal deviation between experimental and numerical results at this stage confirms that the initial stiffness and folding kinematics are accurately captured.

Moving to the second row, corresponding to the intermediate compression stage, more distinct folding emerges in the experimental and simulation images. The Miura cells begin collapsing in a controlled, progressive manner. In the simulation, von Mises stress contours are distributed diagonally from the fold tips toward the center, suggesting plastic hinge formation. The DIC result in this stage reveals denser and more chaotic vector fields around folding intersections, yet still aligned along the global folding pattern. This indicates that energy absorption is actively occurring through local folding and deformation, validating the predictive capability of the finite element model.

In the final row, representing the advanced collapse stage, the simulation shows significant material compaction and stress saturation at upper fold junctions, aligning well with the fully folded experimental sample. Localized buckling is visible in the experimental and DIC images, particularly near the top and bottom ends, where confinement is greatest. DIC vectors at this point exhibit multidirectional strain gradients, indicative of plastic flow and complex strain localization. This confirms that the structure has exceeded its elastic range and is undergoing post-buckling deformation. The simulation successfully predicts this pattern, though slight deviations exist due to imperfections in the printed sample that are not simulated numerically.

Figure 11 confirms high agreement between simulation, experimental, and DIC data. Notably, the DIC results validate the deformation zones and the directional strain flow along the Miura folds. Visualizing vector directions corresponding closely with fold orientations highlights the functional benefit of prefolded geometry in guiding controlled energy absorption. This tri-modal analysis underscores the accuracy of the numerical approach while reinforcing the importance of experimental and DIC validation in capturing real-world manufacturing imperfections and strain heterogeneity.

5 Discussion

The methodology implemented in this study offers significant advancements over previous investigations into origami-based thin-walled structures. Several prior studies serve as benchmarks for comparison, e.g., Deng et al. [55], who explored tubular origami configurations for crashworthiness but limited their scope to axial buckling simulations, lacking experimental correlation. Jiang et al. [56] employed Miura fold patterns for thin-walled structures and identified folding benefits in load management; however, their study relied solely on numerical validation.

Similarly, Zhang et al. [57] proposed zig-zag origami crash boxes fabricated by metal forming, but their analysis lacked optimization and did not assess additive manufacturing feasibility extensively. Wang et al. [58], while investigating Miura-pattern crash tubes via experimental drop tests, focused mainly on deformation patterns without integrating multi-objective optimization or advanced dimensional validation.

In contrast, the present study integrates full experimental validation (including DIC and 3D scanning) with Taguchi-based multi-objective optimization. This comprehensive approach ensures that design decisions are optimal in simulation and manufacturable and effective in real-world conditions. The main strength of the methodology is its robust combination of multi-objective optimization with experimental validation; an approach rarely applied in prior studies on Miura origami crash structures. The Taguchi L27 array reduces experimental complexity while preserving geometric and material variables' sensitivity.

Additionally, including PCA allows for an integrated evaluation of multiple performance criteria. However, some limitations are acknowledged. The study focuses on nine Miura configurations, limiting broader generalization. Also, PCA may mask interactions between correlated metrics. Future work should explore dynamic impact scenarios and broader geometry ranges to fully harness the potential of Miura origami-based energy absorbers.

The scientific novelty of this work lies in its holistic, multi-phase methodology that combines structural design, material testing, Taguchi optimization, numerical simulation, and experimental validation. The study achieves superior balance across critical crashworthiness metrics by adopting a multi-objective optimization framework. Integrating dimensional scanning and DIC enhances result fidelity, allowing for detailed error quantification and practical feedback. These advancements provide a reliable design pipeline for high-performance, additively manufactured crash energy absorbers based on Miura origami thin-walled principles.

6 Conclusions

Based on the analysis of Miura origami thin-walled structures fabricated using selective laser melting (SLM), several key conclusions can be drawn regarding the influence of design parameters on energy absorption capacity, structural stability, and material performance under compressive loading. Analysis of variance (ANOVA) results showed that thickness is the most influential factor, contributing 67 % to energy available (EA), followed by the guiding circle diameter at 14 %, and number of sides at 7 %. While useful for force distribution, segment height only contributed 0.5 %, indicating a relatively minor effect on EA. Similar patterns were observed across other performance metrics, with thickness dominating peak crushing force (PCF) and average force (AF), while the number of sides and the guiding circle diameter moderately affected specific energy absorption (SEA) and AF.

Increasing thickness enhances the moment of inertia and critical load, strengthening the structure's resistance to buckling. However, thicker materials also increase stiffness, which may reduce the energy absorption rate. The n influences the force distribution by creating a more complex folding pattern, which helps distribute forces more evenly and leads to more gradual deformation. The

guiding circle diameter directly affects the effective length of the structure, reducing critical load but allowing greater deformation, thus improving energy absorption. Segment height helps distribute forces more evenly, enhancing energy dissipation. Overall, the design configuration $t_3n_1d_3M_2$ provides the best performance across all testing aspects. The $t_3n_1d_3M_2$ model exhibits optimal performance in EA, SEA, average force, PCF, and crush force efficiency (CFE). This model perfectly balances energy absorption, resistance to compressive loading, and efficient force distribution, making it the best design for energy absorption applications and crash safety. The combination of thickness, number of sides, the guiding circle diameter, and segment height results in a design that not only withstands peak compressive forces but also distributes forces evenly, ensuring better performance in energy absorption during compression.

The 3D scanning results reveal dimensional deviations in the printed structure fabricated by SLM, especially at thinner regions such as the fold points, with deviations ranging from ±0.1 mm to ±0.4 mm in these areas. Compression testing of the AlSi10Mg material shows that, although the material is elastically resistant at the onset, porosity and residual stresses from the SLM process make the material more prone to localized failure and micro-crack initiation in specific regions. These results highlight the need for further optimization of printing parameters to enhance the accuracy and mechanical properties of the material. By optimizing design parameters and adjusting SLM settings, the $t_3n_1d_3M_2$ design can maximize energy absorption, resistance to compressive loads, and efficient force distribution, making it an ideal choice for vehicle safety and structures requiring high energy absorption.

For future research, it is recommended to incorporate post-processing treatments (particularly heat treatment methods such as stress relief annealing or heat treatment) into the fabrication process of SLM-printed thin-walled structures. These treatments have the potential to significantly reduce residual stress, improve microstructural homogeneity, and enhance the ductility and toughness of AlSi10Mg components. Investigating the effects of such treatments on both mechanical performance and dimensional stability would provide valuable insights into optimizing the crashworthiness of origami-inspired designs.

Exploring various heat treatment durations and temperatures could also lead to tailored property enhancement strategies suitable for thin-walled energy-absorbing structures under dynamic and quasi-static loading conditions.

Acknowledgment

The authors express sincere gratitude to the Indonesian Education Scholarship (BPI), the Center for Higher Education Funding and Assessment (PPAPT), the Indonesia Endowment Fund for Education (LPDP), the Higher Education Financing Center (BPPT), and the Ministry of Finance of the Republic of Indonesia for awarding the scholarship and supporting this research.

References

1. Ha, N.S., Lu, G. (2025). A review of recent research on bio-inspired structures and materials for energy absorption applications. *International Composites Part B: Engineering*, Vol. 181, 107496. https://doi.org/10.1016/j.compositesb.2019.107496
2. Hou, S., Li, Q., Long, S., Yang, X., Li, W. (2007). Design optimization of regular hexagonal thin-walled columns with crashworthiness criteria. *Finite Elements in Analysis and Design*, Vol. 43(6–7), pp. 555-565. https://doi.org/10.1016/j.finel.2006.12.008
3. Zhou, J., Ruixian, Q., Bingzhi, C. (2019). Energy absorption properties of multi-cell thin-walled tubes with a double surface gradient. *Thin-Walled Structures*, Vol. 145, 106386. https://doi.org/10.1016/j.tws.2019.106386
4. Kshirsagar, M., Ambike, S.D., Prakash, N.J., Kandasubramanian, B., Deshpande, P. (2023). Origami engineering: Creating dynamic functional materials through folded structures. *Hybrid Advances*, Vol. 4, 100092. https://doi.org/10.1016/j.hybadv.2023.100092
5. Yan, P., Huang, H., Meloni, M., Li, B., Cai, J. (2025). Mechanical properties inside origami-inspired structures: An overview. *Applied Mechanics Reviews*, Vol. 77(1), 011001. https://doi.org/10.1115/1.4066566
6. Yasuda, H., Yang, J. (2015). Reentrant origami-based metamaterials with negative Poisson's ratio and bistability. *Physical Review Letters*, Vol. 114, 185502. https://doi.org/10.1103/PhysRevLett.114.185502
7. Ye, H., Liu, Q., Cheng, J., Li, H., Jian, B., Wang, R., Sun, Z., Lu, Y., Ge, Q. (2023). Multimaterial 3D printed self-locking thick-panel origami metamaterials. *Nature Communications*, Vol. 14, 1607. https://doi.org/10.1038/s41467-023-37343-w
8. Schenk, M., Viquerat, A.D., Seffen, K.A., Guest, S.D. (2014). Review of inflatable booms for deployable space structures: Packing and rigidization. *Journal of Spacecraft and Rockets*, Vol. 51(3), pp. 1–47. https://doi.org/10.2514/1.A32598
9. Sun, Q., Sun, J., Guo, K., Liu, J. (2022). Investigation on mechanical properties and energy absorption capabilities of AlSi10Mg triply periodic minimal surface sheet structures fabricated via selective laser melting. *Journal of Materials Engineering and Performance*, Vol. 31, pp. 9110–9121. https://doi.org/10.1007/s11665-022-06883-5
10. Gebhardt, U., Gustmann, T., Giebeler, L., Hirsch, F., Hufenbach, J.K., Kästner, M. (2022). Additively manufactured AlSi10Mg lattices – Potential and limits of modelling as-designed structures. *Materials & Design*, Vol. 220, 110796. https://doi.org/10.1016/j.matdes.2022.110796
11. Kim, H.-S. (2002). New extruded multi-cell aluminum profile for maximum crash energy absorption and weight efficiency. *Thin-Walled Structures*, Vol. 40(4), pp. 311–327. https://doi.org/10.1016/S0263-8231(01)00069-6

12. Maconachie, T., Leary, M., Lozanovski, B., Zhang, X., Qian, M., Faruque, O., Brandt, M. (2019). SLM lattice structures: Properties, performance, applications and challenges. *Materials & Design*, Vol. 183, 108137. https://doi.org/10.1016/j.matdes.2019.108137
13. Layeb, N., Barhoumi, N., Oldal, I., Keppler, I. (2025). Improving the strength properties of PLA acetabular liners by optimizing FDM 3D printing: Taguchi approach and finite element analysis validation. *The International Journal of Advanced Manufacturing Technology*, Vol. 137, 2649–2664. https://doi.org/10.1007/s00170-025-15314-3
14. Roy, K.R. (2016). *A Primer on the Taguchi Method*. Society of Manufacturing Engineers, Southfield, MI, USA.
15. Antony, J. (2014). *Design of Experiments for Engineers and Scientists*. Elsevier, Amsterdam, Netherlands. https://doi.org/10.1016/C2012-0-03558-2
16. Jolliffe, I.T., Cadima, J. (2016). Principal component analysis: A review and recent developments. *Philosophical Transactions of the Royal Society A: Mathematical, Physical and Engineering Sciences*, Vol. 374(2065), 20150202. https://doi.org/10.1098/rsta.2015.0202
17. Derringer, G., Suich, R. (1980). Simultaneous optimization of several response variables. *Journal of Quality Technology*, Vol. 12(4), pp. 214–219. https://doi.org/10.1080/00224065.1980.11980968
18. Nair, R., Ramachandran, K.I. (2018). Design and optimization of automotive energy absorber structure with functionally graded material. *Materials Today: Proceedings*, Vol. 5(11(3)), pp. 25640–25648. https://doi.org/10.1016/j.matpr.2018.11.005
19. Hussain, K.F., Cantwell, W.J., Khan, K.A. (2025). Review of recent advances in origami-inspired structures for enhanced energy absorption: Trends and engineering applications. *Arabian Journal for Science and Engineering*. https://doi.org/10.1007/s13369-025-10411-7
20. Wierzbicki, T., Abramowicz, W. (1983). On the crushing mechanics of thin-walled structures. *Journal of Applied Mechanics*, Vol. 50(4a), pp. 727–734. https://doi.org/10.1115/1.3167137
21. Allah, M.M.A., El-Baky, M.A.A. (2024). Multi-objective optimization through desirability function analysis on the crashworthiness performance of thermoplastic/thermoset hybrid structures. *Composites Part B: Engineering*, Vol. 284, 111742. https://doi.org/10.1016/j.compositesb.2024.111742
22. Boreanaz, M., Belingardi, G., Maia, C.D.F. (2020). Application of the origami shape in the development of automotive crash box. *Material Design & Processing Communications*, Vol. 2, e181. https://doi.org/10.1002/mdp2.181
23. Miura, M. (1985). Method of packaging and deployment of large sheets of thin material. *Inst. Space Astronaut. Sci. Rep.*, Vol. 618, pp. 1709–1718.
24. Xiang, X.M., Lu, G., You, Z. (2020). Energy absorption of origami inspired structures and materials. *Thin-Walled Structures*, Vol. 157, 107130. https://doi.org/10.1016/j.tws.2020.107130
25. Shiming, W., Yong, P., Tiantian, W., Xuanzhen, C., Lin, H., Honghao, Z. (2019). The origami inspired optimization design to improve the crashworthiness of a multi-cell thin-walled structure for high speed train. *International Journal of Mechanical Sciences*, Vol. 159, pp. 345–358. https://doi.org/10.1016/j.ijmecsci.2019.06.017
26. Li, Z.-H., Nie, Y.-F., Liu, B., Kuai, Z.-Z., Zhao, M., Liu, F. (2020). Mechanical properties of AlSi10Mg lattice structures fabricated by selective laser melting. *Materials & Design*, Vol. 192, 108709. https://doi.org/10.1016/j.matdes.2020.108709
27. Joo, H.M., Kim, W.C., Jung, Y.I., Kim, H.J., Kim, S.J., Jo, Y.C., Yong, W.H., Kim, D.H. (2024). Effect of cell geometry and heat treatment on the energy absorption property of AlSi10Mg alloy lattice structures produced by laser-based powder bed fusion. *Metals and Materials International*, Vol. 30, 1294–1306. https://doi.org/10.1007/s12540-023-01567-8
28. Yasuda, H., Kunimine, T. (2024). Energy absorption of AlSi10Mg origami cellular structures fabricated via laser powder bed fusion. *MRS Communications*, Vol. 14, pp. 496–502. https://doi.org/10.1557/s43579-024-00518-7
29. Madaj, R., Kohar, R., Brumercik, F., Veres, M. (2025). Design study of hole types for improved cooling of experimental heatsinks manufactured by SLM technology using an AlSi10Mg alloy. *Applied Sciences*, Vol. 15(4), 2118. https://doi.org/10.3390/app15042118
30. Bisht, M.S., Gaur, V., Singh, I.V. (2022). On mechanical properties of SLM Al–Si alloy: Role of heat treatment-induced evolution of silicon morphology. *Materials Science and Engineering: A*, Vol. 858, 144157. https://doi.org/10.1016/j.msea.2022.144157
31. Li, J., Qu, M., Jiang, Z. (2023). Multi-objective optimization for 3D printed origami crash box cell based on artificial neural networks and NSGA-II. *Journal of Materials, Processing and Design*, Vol. 7(4), pp. 1–13. https://dx.doi.org/10.23977/jmpd.2023.070401
32. Roy, R.K. (2001). *Design of Experiments Using the Taguchi Approach: 16 Steps to Product and Process Improvement*. John Wiley & Sons, Hoboken, NJ, USA.
33. Du, X., Zhu, F. (2019). A novel principal components analysis (PCA) method for energy absorbing structural design enhanced by data mining. *Advances in Engineering Software*, Vol. 127, pp. 17–27. https://doi.org/10.1016/j.advengsoft.2018.10.005
34. Wang, T., Wang, L., Wang, C., Zou, X. (2018). Crashworthiness analysis and multi-objective optimization of a commercial vehicle frame: A mixed meta-modeling-based method. *Advances in Mechanical Engineering*, Vol. 10(5), pp. 1–12. https://doi.org/10.1177/1687814018778480
35. Manishkumar, M., Desai, C. (2019). A study on design and crash analysis of automotive energy absorption tubes. *Journal of Manufacturing Engineering*, Vol. 14(4), pp. 158–165. https://doi.org/10.37255/jme.v4i4pp158-165
36. Jiang, Z., Rong, J., Chen, Z., Zhu, P., Wei, Z., Wang, S. (2025). Deformation mechanisms and energy absorption characteristics of 3D-printed negative Poisson's ratio sandwich structures subjected to underwater impulsive loading. *International Journal of Impact Engineering*, Vol. 203, 105355. https://doi.org/10.1016/j.ijimpeng.2025.105355

37. Qiang, W., Durandet, Y., Zhang, X., Lu, G. (2024). Experimental and numerical study on energy absorption performance of truncated origami materials. *Thin-Walled Structures*, Vol. 200, 111911. https://doi.org/10.1016/j.tws.2024.111911
38. Kempen, K., Thijs, L., Van Humbeeck, J., Kruth, J.-P. (2012). Mechanical properties of AlSi10Mg produced by selective laser melting. *Physics Procedia*, Vol. 39, pp. 439–446. https://doi.org/10.1016/j.phpro.2012.10.059
39. Jiang, Z., Sun, J., Berto, F., Wang, X., Qian, G. (2023). Fatigue and fracture behavior of AlSi10Mg manufactured by selective laser melting: A review. *Physical Mesomechanics*, Vol. 26, pp. 367–390. https://doi.org/10.1134/S102995992304001X
40. Li, W., Li, S., Liu, J., Zhang, A., Zhou, Y., Wei, Q., Yan, C., Shi, Y. (2016). Effect of heat treatment on AlSi10Mg alloy fabricated by selective laser melting: Microstructure evolution, mechanical properties and fracture mechanism. *Materials Science & Engineering A*, Vol. 663, pp. 116–125. https://doi.org/10.1016/j.msea.2016.03.088
41. Praneeth, J., Venkatesh, S., Krishna, L.S. (2023). Process parameters influence on mechanical properties of AlSi10Mg by SLM. *Materials Today: Proceedings*. https://doi.org/10.1016/j.matpr.2022.12.222
42. Leary, M., Mazur, M., Elambasseril, J., McMillan, M., Chirent, T., Sun, Y., Qian, M., Easton, M., Brandt, M. (2016). Selective laser melting (SLM) of AlSi12Mg lattice structures. *Materials & Design*, Vol. 98, pp. 344–357. https://doi.org/10.1016/j.matdes.2016.02.127
43. Araújo, L.C., Gabriel, A.H.G., da Fonseca, E.B., Avila, J.A., Jardini, A.L., Junior, R.S., Lopes, É.S.N. (2022). Effects of build orientation and heat treatments on the tensile and fracture toughness properties of additively manufactured AlSi10Mg. *International Journal of Mechanical Sciences*, Vol. 213, 106868. https://doi.org/10.1016/j.ijmecsci.2021.106868
44. Limbasiya, N., Jain, A., Soni, H., Wankhede, V., Krolczyk, G., Sahlot, P. (2022). A comprehensive review on the effect of process parameters and post-process treatments on microstructure and mechanical properties of selective laser melting of AlSi10Mg. *Journal of Materials Research and Technology*, Vol. 21, pp. 1141–1176. https://doi.org/10.1016/j.jmrt.2022.09.092
45. Singh, M., Arjunan, A., Baroutaji, A., Wanniarachchi, C.T., Praveen, A.S., Robinson, J., Vance, A., Appiah, M., Arafat, A. (2025). Targeted mechanical and energy absorption properties of 3D printed aluminium metamaterials. *Next Materials*, Vol. 7, 100356. https://doi.org/10.1016/j.nxmate.2024.100356
46. Liu, Y. (2008). ANSYS and LS-DYNA used for structural analysis. *International Journal of Computer Aided Engineering and Technology*, Vol. 1(1), 021254. https://doi.org/10.1504/IJCAET.2008.021254
47. Hu, W. (2023). *Time-Dependent Reliability Analysis*. Springer, Cham, Switzerland. https://doi.org/10.1007/978-3-031-49208-2_6
48. Yadroitsev, I., Smurov, I. (2010). Selective laser melting technology: From the single laser melted track stability to 3D parts of complex shape. *Physics Procedia*, Vol. 5(B), pp. 551–560. https://doi.org/10.1016/j.phpro.2010.08.083
49. Tuković, Ž., Ivanković, A., Karač, A. (2012). Finite-volume stress analysis in multi-material linear elastic body. *International Journal for Numerical Methods in Engineering*, Vol. 93(4), pp. 400–419. https://doi.org/10.1002/nme.4390
50. Liu, K., Paulino, G.H. (2017). Nonlinear mechanics of non-rigid origami: An efficient computational approach. *Proceedings of the Royal Society A: Mathematical, Physical and Engineering Sciences*, Vol. 473(2206), 20170348. https://doi.org/10.1098/rspa.2017.0348
51. Taguchi, G. (1986). *Introduction to Quality Engineering: Designing Quality into Products and Processes*. Asian Productivity Organization, Tokyo, Japan.
52. Harrington, E. C. (1965). The desirability function. *Industrial Quality Control*, Vol. 21, pp. 494–498.
53. Jolliffe, I.T. (2002). *Principal Component Analysis*. Springer, New York, NY, USA. https://doi.org/10.1007/b98835
54. Hussain, S., Qazi, M.I., Abas, M. (2024). Investigation and optimization of plasma arc cutting process parameters for AISI 304 by integrating principal component analysis and composite desirability method. *Journal of the Brazilian Society of Mechanical Sciences and Engineering*, Vol. 46, 33. https://doi.org/10.1007/s40430-023-04614-y
55. Deng, X., Liu, W., Lin, Z. (2018). Experimental and theoretical study on crashworthiness of star-shaped tubes under axial compression. *Thin-Walled Structures*, Vol. 130, pp. 321–331. https://doi.org/10.1016/j.tws.2018.06.002
56. Jiang, B., Gao, W., Xie, Z., Pasini, D., Tan, H. (2025). Thin-walled tubular structures integrating origami patterns and tension-dominated bulkheads for enhanced energy absorption. *Thin-Walled Structures*, Vol. 215(A), 113433. https://doi.org/10.1016/j.tws.2025.113433
57. Zhang, J., Karagiozova, D., Lu, G., Chen, P. (2021). Quasi-static in-plane compression of zig-zag folded metamaterials at large plastic strains. *Thin-Walled Structures*, Vol. 159, 107285. https://doi.org/10.1016/j.tws.2020.107285
58. Wang, G., Li, Z., Lu, Z., Liu, J. (2024). Local impact resistance of curved sandwich panel with Miura-ori foldcore. *Engineering Structures*, Vol. 300, 117232. https://doi.org/10.1016/j.engstruct.2023.117232